Journal of Magnetic Resonance 210 (2011) 200–209

Contents lists available at ScienceDirect

Journal of Magnetic Resonance

journal homepage: www.elsevier.com/locate/jmr

Accurate determination of the spin Hamiltonian parameters for Mn^{2+} ions in cubic ZnS nanocrystals by multifrequency EPR spectra analysis

M. Stefan *, S.V. Nistor, J.N. Barascu

National Institute of Materials Physics, POB MG-7, 077125 Magurele-Bucharest, Romania

ARTICLE INFO

Article history:
Received 18 October 2010
Revised 21 January 2011
Available online 8 March 2011

Keywords:
EPR
Mn^{2+}
Cubic ZnS nanocrystals
EPR line shape simulation

ABSTRACT

Accurate determination of the spin Hamiltonian (SH) parameters, describing the electron paramagnetic resonance (EPR) spectra of paramagnetic impurity ions in wide band gap semiconductor nanocrystals, is essential for determining their localization and quantum properties. Here we present a procedure, based on publicly available software, for determining with higher accuracy the SH parameters of isolated Mn^{2+} impurity ions in small cubic ZnS nanocrystals. The procedure, which can be applied to other cubic II–VI semiconductor nanocrystals as well, is based on the analysis of both low and high frequency EPR spectra with line shape simulation and fitting computing programs, which include the hyperfine forbidden transitions and line broadening effects. The difficulties, limitations and errors which can affect the accuracy in determining some of the SH parameters are also discussed.

1. Introduction

Dopants play a key role in providing alternative means for controlling the remarkable properties of the semiconducting nanocrystals (NCs) associated with the quantum confinement effect (QCE). In the case of nanocrystalline II–VI semiconductors, usually prepared at relatively low temperatures (<350 °C), the mechanisms responsible for the incorporation of isoelectronic impurity ions such as Mn^{2+} or Co^{2+} are still hotly debated after more than 20 years of investigations [1,2]. Moreover, even in the case of cubic ZnS (cZnS) NCs doped with transition ions, a material well known for its outstanding optoelectronic properties, the results concerning the influence of the QCE on its optical properties are contradictory [3–5]. To better understand these properties, essential for any further industrial applications, one needs to know the exact localization of the activating ions in the NCs, the structure of the neighboring ligands.

Electron paramagnetic resonance (EPR) spectroscopy can provide essential information concerning the location of the paramagnetic impurities in the semiconductor crystal lattice and their ground electronic state properties [6]. To reach this goal one firstly needs to determine accurate values of the spin Hamiltonian (SH) parameters which describe the observed spectra. Previous EPR investigations on nanocrystalline cZnS doped with Mn^{2+} ions resulted in the observation of several isolated Mn^{2+} type paramagnetic species [7–12]. However, the differences in the reported SH parameter values raise questions if they were genuine or resulting from the lower accuracy of their determination, as some of the Mn^{2+} centers with close SH parameter values could actually correspond to the same structure. Thus, even in the case of the centers with g-factors and hyperfine parameter values around $g = 2.002$ and $|A| = 64 \times 10^{-4}\,cm^{-1}$, close to those of the substitutional Mn^{2+} ions in the cubic ZnS single crystals (SCs), which are expected to be localized at Zn^{2+} cation sites with T_d local symmetry [13], additional non-cubic zero field splitting (*ZFS*) terms, characterized by the axial D and even rhombic E parameters, with values spread over a two orders of magnitude range, were reported [8,10–12]. No convincing explanation for the presence of such terms was offered. In the case of the other centers with larger hyperfine splittings, attributed to Mn^{2+} ions localized at the surface of the cZnS NCs, the large errors in determining their SH values could also lead to erroneous structure identification.

Therefore, any further progress in determining the exact structure/localization of the Mn^{2+} centers in the cZnS NCs, at both substitutional and surface sites, is conditioned by an increased accuracy in determining the SH parameters. This is a difficult task considering that many characteristic features of such polycrystalline type spectra are wiped out not only by the spatial averaging, but also by the strong line broadening due to the increased crystal lattice disorder, characteristic for nanomaterials [7,14,15]. Thus the efforts had to be directed to both obtaining nanocrystalline materials with a lower degree of lattice disorder, resulting in EPR spectra with narrower lines and better resolution, and improving the quantitative analysis of the recorded EPR spectra.

We have recently shown that EPR spectra of Mn^{2+} impurity ions with improved resolution can be obtained by self-assembling small

* Corresponding author. Fax: +40 21 3690177.
E-mail address: mstefan@infim.ro (M. Stefan).

1090-7807/$ - see front matter © 2011 Elsevier Inc. All rights reserved.
doi:10.1016/j.jmr.2011.03.004

cZnS NCs into a mesoporous structure. Based on a simple analysis of the X-band spectra, three types of isolated Mn^{2+} centers were identified in such samples and tentative values for the *g*- and *A*-parameters were reported [16,17]. Later on we have developed a more precise procedure for the determination of the SH parameters of the Mn(I) center localized in the core of the cZnS NCs from the EPR spectra measured at two microwave frequencies. The procedure was based on the simulation and fitting of the line shape of the experimental EPR spectra, including the analysis of the hyperfine forbidden transitions and line broadening effects, by using publicly available software. Besides determining accurate values for the isotropic Zeeman and hyperfine parameters, we were able to confirm the presence of an axial *ZFS* term with $|D| = 41 \times 10^{-4}\ cm^{-1}$ [18]. From its close SH parameter values with those of the substitutional trigonal Mn^{2+} center (the PN center) in mixed polytype ZnS SCs [19–21], we explained the local axial distortion at the substitutional Mn^{2+} ion in the core of the cZnS NCs as due to its localization next to an extended stacking defect. The proposed model was further supported by a high resolution electron transmission microscopy (HRTEM) study on the same mesoporous cZnS:Mn samples. Because the main focus of that paper has been the determination of the localization of the Mn(I) centers, the surface centers were not discussed and the method employed in obtaining the SH parameters was not detailed.

The present paper gives a detailed description of the two-steps line shape simulation procedure used to determine accurate SH parameter values from the EPR spectra recorded at both low (X) and high (W) microwave frequencies, illustrated for the case of the mesoporous cZnS:Mn nanocrystalline powder. An important part is dedicated to the analysis of the line broadening mechanisms, based on the results of a similar line shape analysis for the EPR spectrum from a micron sized powder sample obtained by crushing a high quality cZnS:Mn SC. By applying this procedure to the three Mn^{2+} centers observed in our cZnS:Mn NCs we were able to obtain a very good fitting of the experimental spectra, which did allow us to determine the specific localization of the Mn^{2+} ions in the observed centers. A discussion of the difficulties and limitations in determining with high accuracy the various SH parameters of the Mn^{2+} centers in cubic nanocrystals by the presented procedure is also included.

2. Results and discussions

2.1. EPR spectra of the Mn^{2+} centers in nanocrystalline cZnS:Mn

The EPR spectrum of the Mn^{2+} ions reported in various cubic ZnS nanocrystalline materials consists of sets of six lines from the allowed central hyperfine transitions with characteristic separations and line widths [7–12,16,17]. Each set of lines corresponds to Mn^{2+} ions in a certain location in the nanomaterial, and, for higher doping levels, in various aggregation states. At lower manganese doping levels (under 0.5% mol), of interest in the present work, the spectra are usually better resolved, due to decreased dipolar broadening, resulting in smaller line width values. In the case of the presently investigated mesoporous, nanocrystalline cZnS doped with 0.2% mol manganese, the EPR spectra consisted of three partially superposed sets of allowed central hyperfine transitions (M_S: $-1/2 \leftrightarrow +1/2$, $\Delta M_I = 0$) attributed to the distinct Mn(I), Mn(II) and Mn(III) centers, corresponding to different localizations of the Mn^{2+} ions in the nanocrystalline material [16–18]. In all cases the non-central transitions (M_S: $\pm1/2 \leftrightarrow \pm3/2, \pm3/2 \leftrightarrow \pm5/2$, $\Delta M_I = 0$) are completely smoothed out (Fig. 1), a feature further explained by the strong line broadening effects. The three spectra are quite well separated, even in the X-band, due to the small line width values, e.g. 0.4 mT in the case of the substitutional

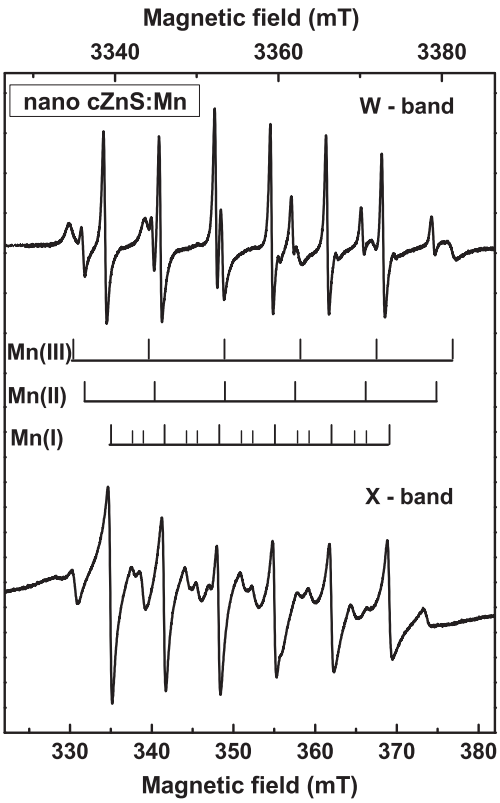

Fig. 1. X- and W-band EPR spectra of the cZnS:Mn nanopowder. The transitions belonging to the three Mn^{2+} centers from the nanopowder are marked with vertical lines.

Mn(I) centers, which is 50% less than the previously reported smallest value of 0.6 mT [11].

The proposed localization of the Mn^{2+} ions corresponding to the three centers was based on the preliminary values of the *g* and *A* parameters, as well as on their behavior under annealing. The most intense Mn(I) spectrum, with the narrowest component lines and *g* and *A* parameters close to those found in cZnS SCs [13], which remains unaffected by annealing up to 200 °C, was attributed to Mn^{2+} ions substituting Zn^{2+} ions at the core of the cZnS nanocrystals. The Mn(I) spectrum also exhibits ten forbidden central hyperfine transitions (M_S: $-1/2 \leftrightarrow +1/2$, $\Delta M_I = \pm1$) of a much larger relative intensity than in the spectrum of the substitutional Mn^{2+} ions in cZnS polycrystalline powder (Fig. 2). As will be further shown, such larger intensity reflects the presence of a supplementary non-cubic local crystal field component at the substitutional Mn^{2+} ions in the core of the cZnS nanocrystals.

The other two Mn(II) and Mn(III) centers, which are sensitive to the thermal history of the sample, were attributed to Mn^{2+} ions localized on the NCs surface [17]. From pulse annealing experiments it was observed that the Mn(III) centers transform into Mn(II) centers during heating, by the temperature activated desorption of neighboring water molecules [17].

As expected, the spectra of the three Mn^{2+} centers in the mesoporous cZnS are better separated at the higher microwave frequency, in the W-band (Fig. 1). This, together with the increased magnetic field resolution, allows a more precise reading of the transition fields. Moreover, the forbidden transitions of the Mn(I) centers are practically unobservable in the W-band spectrum, as the intensity ratio of the forbidden *vs.* allowed hyperfine transitions I_f/I_a is proportional to $D^2/(g\mu_B B)^2$, where μ_B is the Bohr magneton and *B* is the applied static magnetic field [22]. No further improvement in the spectra resolution in both microwave frequency bands was observed by decreasing the measuring temper-

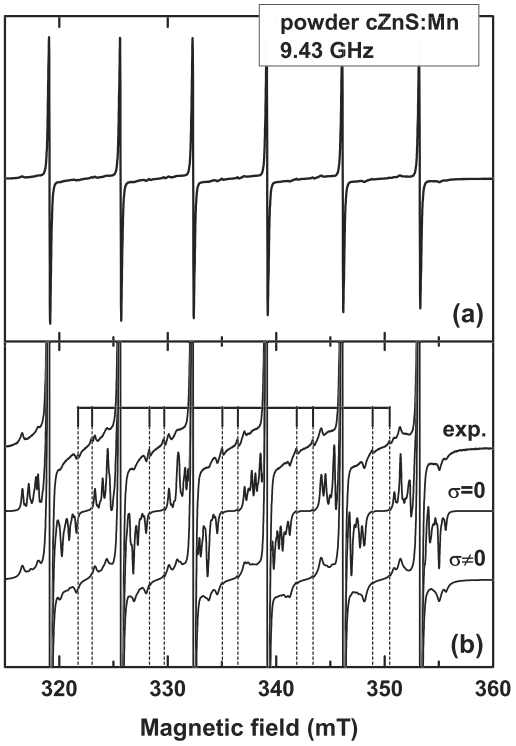

Fig. 2. The X-band EPR spectrum of the polycrystalline cZnS:Mn sample: (a) experimental; (b) detailed view of the broadened non-central transitions in the experimental and simulated (with and without line broadening) spectra. The forbidden transitions are marked with vertical lines.

ature down to 40 K. Therefore the two EPR spectra employed in this study were recorded at RT, in the X (9.87 GHz)- and W (94.04 GHz)-band microwave frequencies, respectively.

2.2. Description of the EPR spectra of Mn^{2+} ions in cubic ZnS (nano) crystals

The EPR spectra of the Mn^{2+} ions embedded in a cubic crystal field with small axial or rhombic distortion are described by the spin Hamiltonian [22]:

$$H = g\mu_B\vec{B}\cdot\vec{S} + A\vec{S}\cdot\vec{I} + H_{ZFS} - g_N\mu_N\vec{B}\cdot\vec{I} \quad (1)$$

Here the first two terms represent the main Zeeman and hyperfine interactions of the $S = 5/2$ electron spin with the external magnetic field B and the $I = 5/2$ nuclear spin of the ^{55}Mn (100% abundance) isotope, respectively. The next *ZFS* term describes the interaction of the electron spin with the local crystal field, while the last term corresponds to the nuclear Zeeman interaction. The *ZFS* term is a sum of the Stevens operators:

$$H_{ZFS} = B_2^0O_2^0 + B_2^2O_2^2 + B_4^0O_4^0 + B_4^mO_4^m \quad (2)$$

where $m = 4$ for the cubic and tetragonal symmetry and $m = 3$ for the trigonal symmetry. For cubic symmetry, in a reference frame with the z axis along a $\langle 0\,0\,1\rangle$ crystalline direction, the second order *ZFS* parameters fulfill the conditions $B_2^0 = D/3 = 0$, $B_2^2 = E = 0$ and $B_4^4 = 5B_4^0$, as is the case in the cZnS SC. If a trigonal reference system is used instead, with the z axis along the $\langle 1\,1\,1\rangle$ crystalline direction, the relations between the *ZFS* parameter values become $B_2^0 = B_2^2 = 0$ and $B_4^3 = 20\sqrt{2}B_4^0$.

The EPR spectra of the Mn^{2+} centers in nanocrystalline cZnS:Mn reported in literature were usually described with the SH (1), where the *ZFS* contribution from a local distortion superimposed on the cubic crystal field was taken as:

$$H_{ZFS} = B_2^0O_2^0 + B_2^2O_2^2 \quad (3)$$

Table 1 presents the previously reported parameter values of the isolated Mn^{2+} ions in cubic ZnS bulk and nanopowders, as well as a few relevant reference data on bulk single crystals. The determinations used only the positions of the six allowed central hyperfine transitions. One can see in the case of the nanocrystalline cZnS a large spread in the reported parameter values, especially for the B_2^0 parameter. This seems very likely to be due to the rough approximations used in their determination, as will be discussed in Section 2.5. However, differences in the SH parameters due to variations in the localization of the Mn^{2+} ions cannot be excluded in all reported cases.

2.3. EPR spectra of Mn^{2+} ions in cZnS crystalline powder: line broadening effects

For cubic single crystals the SH parameters are usually determined by fitting the line positions from spectra recorded at several

Table 1
The EPR parameters of the paramagnetic centers attributed to isolated Mn^{2+} ions in single crystals, powders and nanostructures of ZnS. The measuring microwave frequency band is mentioned next to the line width ΔB_{pp}.

Lattice host/center	g	$\lvert A\rvert$ (10^{-4} cm^{-1})	*ZFS* (10^{-4} cm^{-1})	ΔB_{pp} (mT)	Refs.
cZnS:Mn single crystal/ substitutional Mn^{2+}	2.00225	$A = -63.88$	$z\|\|\langle 0\,0\,1\rangle$: $B_4^0 = 0.0666$, $B_4^4 = 0.3330$. $z\|\|\langle 1\,1\,1\rangle$: $B_4^0 = -0.0444$, $B_4^3 = -1.2558$	0.035 (X)	[13]
Mixed polytype ZnS:Mn crystal/PN	2.0018	$A = -64.9$	$\lvert B_2^0\rvert = 12.03$, $B_4^0 = -0.0411$, $B_4^3 = -1.1549$		[19,20]
Nano ZnS:Mn/NC1	2.003	64.5			[7]
Nano ZnS:Mn/NC2	2.001	89	$\lvert B_2^0\rvert = 167-333$		[7]
Nano ZnS:Mn/S_I	2.001	63.9	$\lvert B_2^0\rvert = 0.3$	0.9 (X)	[8]
Nano ZnS:Mn/S_{II}	2.001	90.0		4.7 (X)	[8]
Nano ZnS:Mn/S_{IV}	2.0025	90.0		20.4 (X)	[8]
Nano ZnS:Mn/Signal I	2.0024	64.5	$\lvert B_2^0\rvert = 30.3$	0.7 (X), 0.45 (Q)	[10]
Nano ZnS:Mn/Signal II	2.0013	84.13	$\lvert B_2^0\rvert = 53.3$	1.08 (Q)	[10]
Nano ZnS:Mn-samples 1, 2	$g_{xx} = 2.0064$, $g_{yy} = 2.0064$, $g_{zz} = 2.0066$	$\lvert A_{xx}\rvert = 63.9$, $\lvert A_{yy}\rvert = 64.0$, $\lvert A_{zz}\rvert = 64.4$	$\lvert B_2^0\rvert = \lvert B_2^2\rvert = 12.47$	0.6 (X)	[11]
Nano ZnS:Mn/sample Ib	$g_\perp = 2.0075$, $g_{\|\|} = 2.004$	$\lvert A_\perp\rvert = 63.8$, $\lvert A_{\|\|}\rvert = 65.2$	$\lvert B_2^0\rvert = \lvert B_2^2\rvert = 12.47$	0.6 (X)	[12]
Nano ZnS:Mn/sample Ih	$g_\perp = 2.006$, $g_{\|\|} = 2.003$	$\lvert A_\perp\rvert = 79.5$, $\lvert A_{\|\|}\rvert = 84.0$	$\lvert B_2^0\rvert = \lvert B_2^2\rvert = 124.6$		[12]
Nano ZnS:Mn/sample SD	$g_\perp = 2.006$, $g_{\|\|} = 2.003$	$\lvert A_\perp\rvert = 79.5$, $\lvert A_{\|\|}\rvert = 84.0$	$\lvert B_2^0\rvert = \lvert B_2^2\rvert = 46.7$		[12]
Nano ZnS:Mn/Mn(I)	2.0020 ± 0.0002	$A = -63.9 \pm 0.4$	$\lvert B_2^0\rvert = 15 \pm 3$	0.4 (X)	[17]
Nano ZnS:Mn/Mn(II)	2.0009 ± 0.0005	$A = -80.6 \pm 0.5$		0.6 (X)	[17]
Nano ZnS:Mn/Mn(III)	2.000 ± 0.002	$A = -87.0 \pm 1.0$		1.5 (X)	[17]

orientations of the magnetic field in a (1 1 0) and/or (1 0 0) crystal plane [6]. Due to the large number of available experimental points/data and to the narrow lines, one can obtain, for well oriented single crystals, full sets of highly accurate SH parameter values, as was recently reported for Mn^{2+} ions in a pure cubic phase ZnS SC [13]. In the case of the nanocrystalline powders, the number of experimental data (as line positions) available for determining the SH parameters is greatly reduced, not only by the spatial averaging of the spectra, but also by the strong line broadening. Until now, this latter effect has been very little taken into consideration for this particular case. Therefore, due to the important role that the line broadening plays in the determination of the SH parameters in nanocrystals, we shall firstly discuss its importance and role in the line shape simulations of the EPR spectra of the Mn^{2+} in crystalline powders.

The EPR line broadening effect has been observed even in single crystals of high structural perfection doped with Mn^{2+}, such as calcite [23], tungstates [24–26] or cZnS [13]. Its presence was attributed to random strains, electrical fields and other perturbations from the extended lattice defects in the crystal lattice [27], resulting in a variation in the local crystal field at the paramagnetic ions, both in magnitude and orientation.

In a previous investigation of two cZnS SCs [13], one nominally pure and the other doped in the melt with 0.5% $MnCl_2$, we have observed in both crystals EPR spectra from Mn^{2+} ions localized substitutionally at the tetrahedral Zn^{2+} sites, in a concentration ratio of ~1/1000. The observed broadening of the EPR lines corresponding to the allowed non-central transitions (M_S: ±1/2 ↔ ±3/2, ±3/2 ↔ ±5/2, $\Delta M_I = 0$) from the Mn^{2+} spectra was explained by fluctuations in the EPR parameter values induced by a random distribution of lattice strains. For the allowed central transitions (M_S: −1/2 ↔ +1/2, $\Delta M_I = 0$) the isotropic line width depended solely on the manganese concentration, being ~2.5 times larger for the manganese doped SC compared with the nominally pure one. This effect was attributed to the increased dipolar interaction, at higher concentrations, between the Mn^{2+} ions embedded in the crystal lattice. The following analysis of the line broadening effects in a polycrystalline cZnS:Mn sample obtained by crushing a manganese doped cZnS SC is based on this result.

The X-band EPR spectrum of the crushed/polycrystalline sample is displayed in Fig. 2a. It exhibits, between the very intense six intense allowed central hyperfine transitions, five pairs of lines from the forbidden non-central hyperfine transitions (M_S: −1/2 ↔ +1/2, $\Delta M_I = \pm 1$), marked with vertical lines in Fig. 2b. These transitions are noticeably less intense relative to the allowed central transitions compared to the nanocrystalline cZnS (Fig. 1 – X-band spectrum). Several lines of intensity comparable to the intensity of the forbidden transitions, corresponding to the allowed non-central transitions, are also visible, unlike in the NCs case.

The simulated spectrum, obtained with the cZnS SC parameter values from Ref. [13], without line broadening effects, is given in Fig. 2b ($\sigma = 0$). One can see that the line positions from the simulated spectrum are in very good agreement with the line positions from the experimental spectrum. However, the simulated spectrum also exhibits around each intense allowed central transition several additional lines resulting from the allowed non-central transitions. Not only the number, but also the intensity of these lines in the simulated spectrum is different from the experimental spectrum, an effect which is attributed to the line broadening.

Our attempts to reproduce the line broadening in the polycrystalline sample spectrum by including fluctuations in the cubic (B_4^0, B_4^4) and axial B_2^0 parameter values in the line shape simulation, based on the similar SC analysis [13], were not successful. Therefore we had to take into consideration the fact that new strains were induced during the crushing of the cZnS:Mn SCs. We found out that the best fit with the experimental spectrum was obtained by considering the presence of trigonal distortions in the polycrystalline sample (Fig. 2b, $\sigma \neq 0$). These distortions were accounted for by including in the simulation procedure Gaussian distributions of the *ZFS* parameters centered on the values of these parameters calculated for cubic symmetry in a trigonal reference system (see Table 1). The standard deviations for the parameter value distributions employed in the simulated spectrum from Fig. 2b are: $\sigma(B_2^0) = 1.27 \times 10^{-4}\ cm^{-1}$, $\sigma(B_4^0) = 0.0085 \times 10^{-4}\ cm^{-1}$ and $\sigma(B_4^3) = 0.085 \times 10^{-4}\ cm^{-1}$.

One should notice that although the positions, amplitudes and line widths of the allowed transitions are quite well reproduced in the spectrum simulated with this model, the forbidden hyperfine transitions intensity is much lower (about nine times) in the simulated spectrum than in the experimental one. A similar situation has been observed in the SC spectra [13], where the forbidden transitions in the experimental spectrum were two times more intense than in the simulations, a result which could not be explained in a satisfactory manner. One could only suggest that the much larger difference between the experimental and simulated spectra of Mn^{2+} in the polycrystalline ZnS sample might be due to the presence of other distorted Mn^{2+} centers formed during the crushing process, for which additional non-zero axial *ZFS* terms would contribute to the forbidden transitions intensity.

2.4. Determination of the SH parameters of the Mn^{2+} centers in cZnS:Mn nanopowders

2.4.1. The substitutional Mn(I) centers

The accurate determination of the SH parameters of the Mn^{2+} centers in the cZnS nanocrystals is based on a two steps procedure. Thus, in the first step accurate *g* and *A* parameters, very close to those found in cZnS SCs, were determined by fitting the W-band spectrum with the calculated line positions obtained by neglecting the contribution of the *ZFS* terms, contribution estimated to be within the experimental errors at such high magnetic fields. In the second step, the axial *ZFS* parameter value B_2^0 was obtained by fitting the experimental line shape of the more sensitive X-band spectrum, using the previously determined *g* and *A* values. The possible presence of other *ZFS* terms, as well as of anisotropies in the *g* and *A* values, were also checked in this step.

As starting SH parameters we used the approximate values $g = 2.0020 \pm 0.0002$, $A = -(63.9 \pm 0.4) \times 10^{-4}\ cm^{-1}$ and $|B_2^0| = (15 \pm 3) \times 10^{-4}\ cm^{-1}$, determined by fitting the experimental line positions of the allowed and forbidden central hyperfine transitions from the X-band powder spectrum with the values calculated based on the diagonalization of the SH [17]. A similar procedure was employed in the first step to determine the *g* and *A* parameters from the line positions in the high frequency W-band EPR spectrum, considering only the Zeeman and hyperfine terms. Perturbation calculations up to the third order have shown [28] that in the powder spectra the positions of the observed allowed and forbidden central transitions are influenced by the axial *ZFS* term only in the second [$\sim D^2/(g\mu_B B)$] and third [$\sim AD^2/(g\mu_B B)^2$, $\sim A^2 D/(g\mu_B B)^2$] approximations. As these higher order contributions to the line positions are orientation dependent in a single crystallite, the resulting line width in the powder spectrum is roughly proportional to $D^2/(g\mu_B B)$ [29]. Therefore, for the W-band spectrum, the effect of the *ZFS* terms of moderate magnitude ($|D| = 3|B_2^0| < 50 \times 10^{-4}\ cm^{-1}$) on both line positions and line shape of the central hyperfine transitions is practically negligible, which also explains the narrower component lines at this frequency. The resulting accurate *g*- and *A*-parameter values were further used as fixed values in the simulation of the X-band spectrum in the second step (Table 2).

In the second step we initially performed simulations of the X-band spectrum with a SH consisting of the Zeeman (electronic and

Table 2
The EPR parameters and line width values resulted from fitting the experimental X- and W-band spectra of the Mn^{2+} centers in cZnS NCs.

Center	g	A (10^{-4} cm^{-1})	B_2^0 (10^{-4} cm^{-1})	B_4^m (10^{-4} cm^{-1})	ΔB_{pp} (mT)
Mn(I)	2.0022 ± 0.0001	−63.70 ± 0.05	−13.7 ± 0.9	$B_4^0 = -0.0411$, $B_4^3 = -1.1549$	0.31 (X), 0.34 (W)
Mn(II)	2.0012 ± 0.0002	−80.5 ± 0.2	20–30		0.4 (X, W)
Mn(III)	2.0009 ± 0.0002	−86.8 ± 0.2	25–35		1.1 (X, W)
Mn agglomerates	2.003				29 (X)

nuclear), hyperfine and second order axial *ZFS* terms to find the range of B_2^0-values which were better reproducing the experimental spectrum. As the non-central transitions are wiped out by the lattice disorder/strains, we have restricted our simulations only to the six allowed and ten forbidden central transitions. The resulting simulated spectra were similar enough to those obtained when including all transitions and broadening effects, but the calculation time was much shorter. The determining factors in choosing the appropriate B_2^0 value were the resulting line positions and intensity, as well as the best reproduction of the line shape. Fig. 3a displays the simulations performed for a range of B_2^0 values from 12 to 18×10^{-4} cm^{-1} and a peak-to-peak line width value of 0.31 mT. The Lorentzian line shape was assigned to match the shape of the experimental powder lines. The line shape choice was supported by the results of the EPR study on the cubic ZnS:Mn SCs [13], where the Mn^{2+} spectrum lines were observed to remain isotropic and Lorentzian in shape even when the higher concentration of Mn^{2+} resulted in a dipolar broadening of the lines. The line width input value fits reasonably well the experimental lines for this range of B_2^0 values. For smaller B_2^0 values the line width would have to be increased in order to acquire the match between the simulated and experimental lines.

It is obvious from Fig. 3a that a larger B_2^0 value results in higher forbidden transitions intensity and a better line amplitude ratio reproduction in the simulated spectra, but the line also becomes broader and the line shape is distorted. This last effect is better observed on the higher field lines (Fig. 3a, right hand side). An increase in the input line width in order to cover the line shape distortion would only result in a simulated line width broader than experimentally observed. Taking these opposing effects into consideration, the best fit was found for B_2^0 values around 13.3×10^{-4} cm^{-1}, with an upper limit of 15×10^{-4} cm^{-1}.

The presence of a clearly non-zero axial *ZFS* parameter value proves that the local symmetry at the substitutional Mn(I) center is lower than cubic. Our next goal was to determine the degree of anisotropy, which was reported in a few publications [11,12], by checking the limits for a possible anisotropy in the *g*- and *A*-parameter values, as well as the possible presence of other, non-axial *ZFS* terms. Fig. 3b displays the results of simulations of the X- and W-band spectra performed for $B_2^0 = 14 \times 10^{-4}$ cm^{-1}, by including small axial anisotropies $\Delta g = g_z - g_\perp$ and $\Delta A = A_z - A_\perp$, where $g_\perp = g_x = g_y$ and $A_\perp = A_x = A_y$. Here and in all following simulations the line shape was considered to be Lorentzian, with the $\Delta B_{pp}(X) = 0.31$ mT and $\Delta B_{pp}(W) = 0.34$ mT line width values in the X- and W-band, respectively. The individual line width used for the W-band spectrum simulation matches the experimental peak-to-peak line width, as for such small values of the B_2^0 parameter the higher order contributions are insignificant. We have noticed that the *g*-anisotropy had a stronger effect on the W-band spectrum, while the influence of the *A*-anisotropy was stronger in the X-band spectrum. Therefore, on the left hand side of Fig. 3b we have displayed the highest field line of the W-band spectrum simulated for different values of Δg. One notices that a limiting *g*-anisotropy value, for which the simulated line shape and width are still acceptable, is $\Delta g = 0.0002$. Similarly, in the case of the *A*-anisotropy the limit value is $\Delta A = 0.5 \times 10^{-4}$ cm^{-1}, as one can see from the highest field lines of the simulated X-band spectra on the right hand side of Fig. 3b.

We have also checked the influence on the simulated spectrum of the second order rhombic term and of the fourth order *ZFS* terms, respectively. In the first case we have considered for the rhombic parameter the highest absolute value $|B_2^2| = |B_2^0| = D/3$, according to the standard range of values for the *ZFS* parameters $-1 \leqslant 3E/D \leqslant 0$ determined by Poole et al. [30]. According to the same standard system, D and E and, therefore, B_2^0 and B_2^2, have opposite signs. In the second case, we considered a tetragonal local symmetry, with the B_4^0, B_4^4 parameter values of the Mn^{2+} center in the cubic ZnS SCs [13], as well as a trigonal local symmetry, with the B_4^0, B_4^3 parameter values of the PN center in mixed polytype ZnS [19,20], respectively. Both sets of values are given in Table 1. Because the values of these *ZFS* parameters were too small to influence noticeably the W-band spectrum, the simulations were performed only in the X-band, with the *g*, *A* values from Table 2 and $B_2^0 = -15 \times 10^{-4}$ cm^{-1}. The resulting simulated spectra are displayed in Fig. 3c. A comparison of these simulations with a similar set obtained for $B_2^0 > 0$ showed that the negative sign of B_2^0 results in a better simulation of the relative amplitude ratios of the allowed central transitions.

Indeed, the widths and amplitudes of the simulated powder spectrum lines are affected by the sign of the AB_2^0 parameters product. This is explained by the higher order, orientation dependent, contributions of these parameters to both line positions and intensities of the allowed and forbidden central transitions. Their summed contribution affects differently the powder lines corresponding to distinct values of m [29], giving rise to dissimilar amplitude ratios of the allowed central transitions for the two signs of the AB_2^0 product. Because the sign of the *A* parameter for the Mn^{2+} ions in ZnS is negative [13], it follows that the sign of the B_2^0 parameter can be determined from fitting the pattern of the powder-like spectrum.

In what concerns the other *ZFS* parameters, the only one which seems to make a difference is B_2^2 whose presence determines a slight asymmetry of the lines, but the effect is too small to be distinguished in the experimental spectrum. Therefore, from such simulations we could not ascertain the presence of any other *ZFS* term besides the second order axial one, and could not make a more nuanced statement about the local symmetry at the Mn^{2+} ions.

In order to further improve the accuracy of the line shape simulations we proceeded to the investigation of the line broadening effect, considering the presence of various combinations of *ZFS* terms in the SH and all transitions in the simulated spectra. Fig. 4a and b displays the experimental (top most) spectra followed by the simulated spectra in the X- and W-band, respectively, without (left hand side) and with (right hand side) line broadening included. The simulations were performed with the *g*, *A* and ΔB_{pp} values from Table 2, $B_2^0 = 15 \times 10^{-4}$ cm^{-1}, $B_2^2 = -B_2^0$ and the fourth order *ZFS* parameter values as previously discussed for the tetragonal and trigonal symmetries. One should mention that in the case of the spectra simulated without including line broadening a partial smoothing out of the non-central transitions is noticeable in the case of the rhombic symmetry.

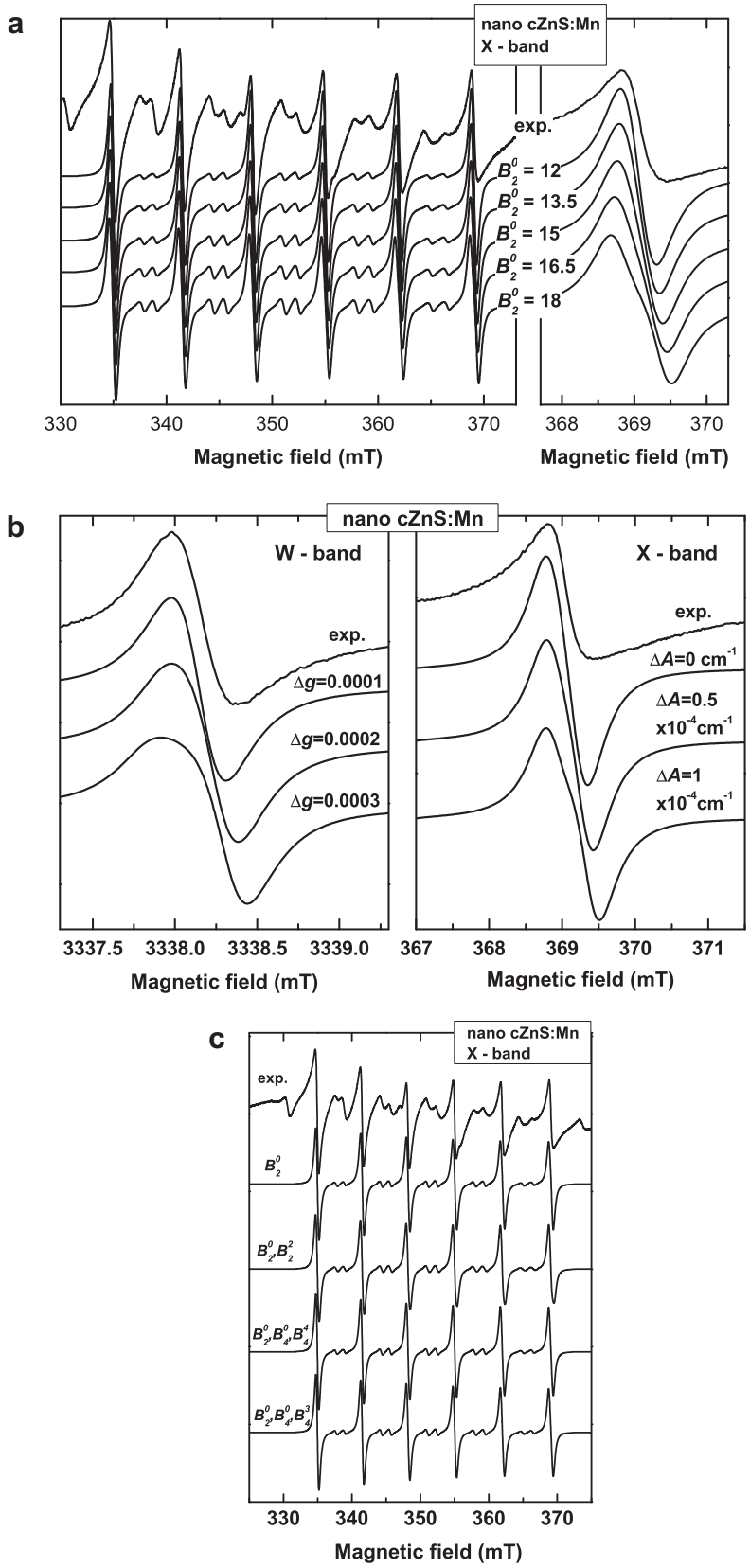

Fig. 3. Experimental and simulated EPR spectra of the Mn(I) center in the mesoporous cZnS:Mn nanopowder. All simulations were performed only for the allowed and forbidden central transitions. (a) Determination of the B_2^0-value. Left: X-band spectrum simulations for different B_2^0-values. Right: detailed view of the highest field line of the spectra. (b) Evaluation of the limits for the *g*- and *A*-anisotropy. Left: W-band spectrum simulations with different Δg values and isotropic *A*-parameter. Right: X-band spectrum simulations with different ΔA values and isotropic *g*-parameter. (c) Evaluation of the effect of the rhombic and fourth order *ZFS* terms on the X-band spectrum. The *ZFS* terms included are mentioned for each spectrum simulation.

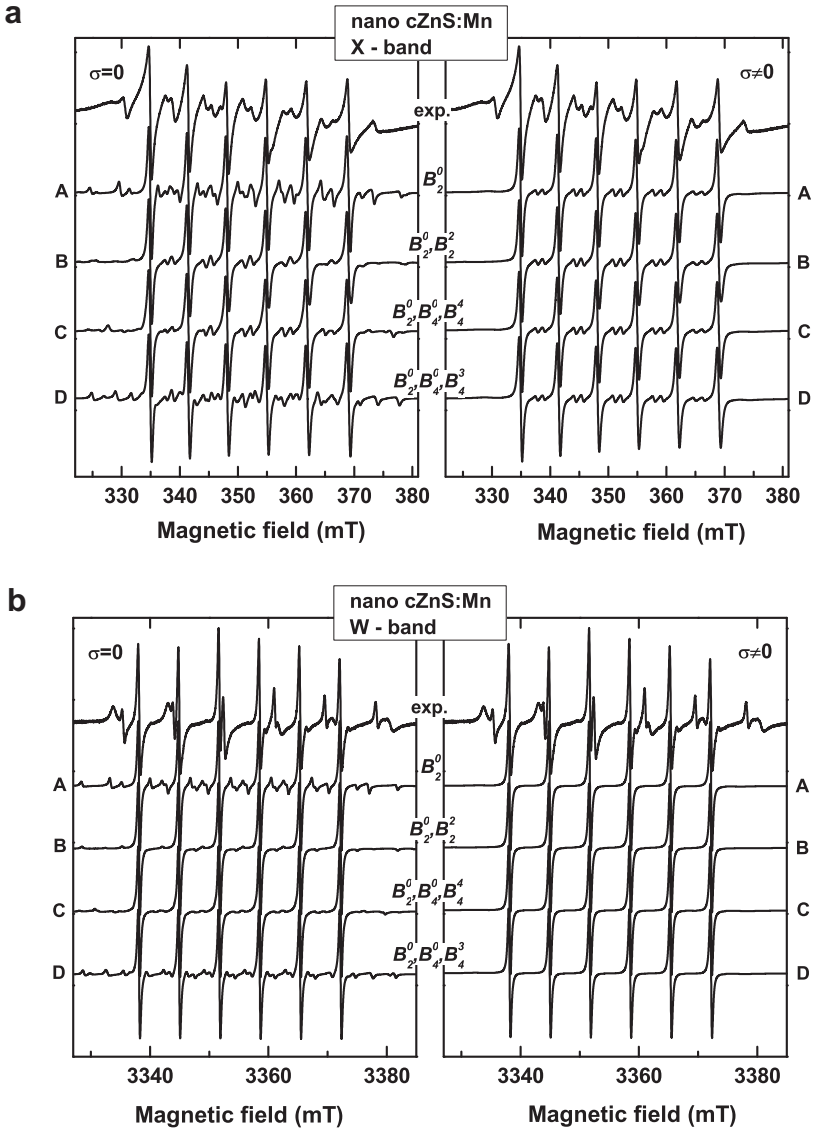

Fig. 4. Experimental and simulated (a) X- and (b) W-band EPR spectra of the Mn(I) center in cZnS:Mn nanopowder. The simulations were performed for different *ZFS* terms by including all transitions, without (left) and with (right) line broadening. The *ZFS* terms included are mentioned for each spectrum simulation.

The line broadening effects were included in the simulations as Gaussian distributions of the different *ZFS* parameter values, centered on the nominal values. The standard deviations of these distributions were determined as the minimum values for which the non-central transitions were wiped out. The *ZFS* parameter distributions were the same for both X- and W-band spectra. The standard deviations of the *ZFS* parameters used for the spectra displayed in the right hand side of Fig. 4a and b were $\sigma(B_2^0) = 6 \times 10^{-4}$ cm^{-1} for the A, C and D spectra and $\sigma(B_2^0) = 4 \times 10^{-4}$ cm^{-1} and $\sigma(B_2^2) = 2 \times 10^{-4}$ cm^{-1} for the B spectra where the rhombic term was included.

In the case of the fourth order parameters we have found that the magnitude of their standard deviations bore little influence on the resulting simulated spectra, whose shapes were mainly dictated by the $\sigma(B_2^0)$ parameter. One can see that the C spectra, with $\sigma(B_4^0) = 0.03 \times 10^{-4}$ cm^{-1}, $\sigma(B_4^4) = 0.15 \times 10^{-4}$ cm^{-1} and D spectra, with $\sigma(B_4^0) = 0.02 \times 10^{-4}$ cm^{-1}, $\sigma(B_4^4) = 0.58 \times 10^{-4}$ cm^{-1}, show no difference from the B spectra. Thus, unlike the case of the micron sized powder sample, for the cZnS:Mn nanopowders we were not able to evidence the influence of the fourth order *ZFS* terms on the EPR spectra.

Comparing the broadened B and A spectra, one can also see that the effect of the B_2^2 parameter on the line shape can be reproduced in the pure axial case by an increase in the value of $\sigma(B_2^0)$. Therefore, the presence/absence of the rhombic distortion in the local field at the Mn(I) centers cannot be ascertained.

A better insight in the structure of the Mn(I) center can be obtained from the analysis of the accurate SH parameters, namely *g*, *A* and B_2^0, given in Table 2. While the *g*- and *A*-values are typical for the Mn^{2+} ions in cubic T_d symmetry [13], the B_2^0 range of values corresponds to the PN-type centers in strongly disordered cZnS SCs, containing various polytypes (Table 1). The PN center was found to consist of a Mn^{2+} ion localized substitutionally at a Zn^{2+} site with a neighboring extended lattice defect, such as a stacking fault or twin, which induced a trigonal distortion [18]. Therefore, the natural choice for the spectra simulation would be the trigonal symmetry. Also, as previously observed in the case of the simulations performed including only the central transitions, for $B_2^0 < 0$ the spectra simulated including all transitions show a better match of the amplitude ratio of the experimental lines than for $B_2^0 > 0$.

According to our simulations, a possible contribution from a sizable amount of substitutional Mn^{2+} ions at pure unperturbed tetra-

hedral sites is unlikely. Indeed, the intensity of the forbidden lines of the cubic centers is negligible, while their allowed central transitions would practically overlap the corresponding lines from the Mn(I) centers, due to the close values of their *g*- and *A*-parameters. The total resulting relative intensity of the forbidden transitions *vs.* the allowed transitions in the simulated spectrum would be thus even smaller than the actually observed ratio, worsening the simulation of the experimental spectrum.

2.4.2. The surface Mn(II) and Mn(III) centers

In the case of the Mn(II) and Mn(III) centers, accurate *g*- and *A*-parameter values were determined by the same two steps procedure as for the Mn(I) centers (Table 2). As their EPR lines overlapped even at high frequency, we initially determined the SH parameters of the Mn(II) centers from the analysis of the W-band spectrum from a sample annealed at 175 °C, containing only the Mn(I) and Mn(II) center lines [18]. The SH parameters of the Mn(III) centers were further obtained from the EPR spectra of a sample containing the lines of all three Mn^{2+} centers.

One should mention that for both surface centers the forbidden central transitions could not be observed in the X-band spectrum, due to the larger line width of ~0.85 mT and ~1.5 mT of the Mn(II) and Mn(III) centers, respectively and the overlap of the more intense Mn(I) centers spectrum. Therefore we could determine only a range of values for the axial B_2^0 parameter for which the broader lines of the X-band spectra were reasonably well reproduced, namely from 20 to 30 for the Mn(II) centers and from 25 to 35 for the Mn(III) centers (in 10^{-4} cm^{-1} units). These values were obtained using as individual line widths in the spectra simulation the corresponding experimental peak-to-peak line widths of the W-band spectrum, of 0.4 mT and 1.1 mT for the Mn(II) and Mn(III) centers, respectively. As the B_2^0 parameter values are small enough to have negligible effects on the W-band spectrum, the experimental line width matches the individual isotropic, Lorentzian-shaped line. For diluted systems, the width of the homogeneously broadened lines usually increases with the measuring microwave frequency, due to changes in the dominant relaxation mechanism from the multiphonon to the one-phonon direct relaxation one [22,31]. Therefore, the individual X-band line width of the Mn^{2+} surface centers is expected to be actually narrower than for the W-band spectra, as observed for the Mn(I) centers.

One should mention that the local symmetry at the Mn^{2+} centers localized on the surface of the NCs is expected to be lower than axial, and the degree of disorder of their environment much higher than for the substitutional Mn(I) centers. Therefore, besides the axial second order term, other *ZFS* terms are expected to be present and the fluctuations in the values of the SH parameters to be considerably larger, in agreement with our spectra analysis.

The final check of the validity of our approach has been the simulation of the entire X- and W-band spectra of the cZnS:Mn nanocrystals. The final calculated spectra (Fig. 5) were obtained as a summation of the simulated spectra of all Mn^{2+} centers. The following parameters were employed in these simulations:

For the Mn(I) center, considered to be of PN type: the *g*, *A* and ΔB_{pp} values from Table 2, $B_2^0 = -14 \times 10^{-4}$ cm^{-1}, $B_4^0 = -0.0411 \times 10^{-4}$ cm^{-1}, $B_4^3 = -1.1549 \times 10^{-4}$ cm^{-1}, $\sigma(B_2^0) = 6 \times 10^{-4}$ cm^{-1}, $\sigma(B_4^0) = 0.02 \times 10^{-4}$ cm^{-1}, $\sigma(B_4^3) = 0.58 \times 10^{-4}$ cm^{-1}.

For the Mn(II) center: the *g*, *A* and ΔB_{pp} values from Table 2, $B_2^0 = 27 \times 10^{-4}$ cm^{-1}, $\sigma(B_2^0) = 17 \times 10^{-4}$ cm^{-1}.

For the Mn(III) center: the *g*, *A* and ΔB_{pp} values from Table 2, $B_2^0 = 30 \times 10^{-4}$ cm^{-1}, $\sigma(B_2^0) = 16 \times 10^{-4}$ cm^{-1}.

Fig. 5 displays the experimental X- and W-band spectra together with the calculated spectra. The fitting is quite good, especially for the W-band spectrum. In the case of the X-band spectrum we were unable to reproduce completely the broadening of the lower part of the allowed transitions of the Mn(I) centers, which is the source of the main differences between the experimental and calculated spectra. We cannot at the moment provide an explanation for this particular shape of the lines.

One should also mention that the experimental X-band spectrum contains a background broad line ($\Delta B_{pp} \approx 29$ mT) centered at $g = 2.003$, better observed for large magnetic field modulation amplitudes, which we attribute to aggregates of remaining doping manganese acetate, very likely left in the nanopores of the mesoporous ZnS. A similar EPR signal was previously observed in the EPR spectra of cZnS powders doped with high concentrations of manganese [32]. This signal was added in our simulations as a Lorentzian line, with the above mentioned parameters and adjusted intensity.

2.5. Comparison with previously reported procedures for the determination of the SH parameters of Mn^{2+} ions in cubic nanocrystals

Our results allow us to underline the significant differences between the Mn^{2+} centers in the crystalline bulk and nanostructured cZnS. The substitutional Mn^{2+} ions in the nanocrystals were found to be localized near an extended defect, unlike in the bulk cZnS where the Mn^{2+} ions enter in cubic Zn^{2+} sites. The neighboring extended defects also seem to be involved in the incorporation/doping process of impurities in such nanocrystals prepared at low temperatures. Also, while a rather large part of the Mn^{2+} ions was found on the nanocrystals surface, no evidence of such centers could be observed in the EPR spectra of the powder cZnS.

Very few attempts have been made up to now to determine the *ZFS* parameters of the Mn^{2+} centers in cZnS nanocrystals. In the case of the substitutional Mn^{2+} ions, to our knowledge only two such studies have been reported. Igarashi et al. [10] have used Allen's method [33], which allows the evaluation of the axial *ZFS* parameter from a second order perturbation calculation of the intensity of the allowed central hyperfine transitions. The resulting $B_2^0 = 30.3 \times 10^{-4}$ cm^{-1} value for their so called Signal I (Table 1) is approximately two times larger than what we obtained for the Mn(I) centers.

Gonzalez Beermann et al. [11,12], which reported the EPR spectra of substitutional Mn^{2+} ions in cZnS nanocrystals with the second narrowest lines (~0.6 mT), have determined the SH parameters by using a line shape simulation procedure which did not include the forbidden transitions and broadening effects. For two types of samples with low concentrations of manganese, called "1" (0.003% Mn) and "2" (0.008% Mn) [11] and "Ib" (0.026% Mn) [12], respectively, they reported different values for the SH parameters, which included anisotropic *g*- and *A*-parameters and a rhombic parameter $|B_2^2| = |B_2^0|$ (Table 1). For all samples the determined *g*-values are considerably larger than those reported up to now for Mn^{2+} in cZnS. Moreover, the reported *A*-parameters, although falling in the range of values expected for substitutional Mn^{2+} centers in ZnS, exhibit, like the *g*-parameters, anisotropies quite difficult to understand for Mn^{2+} ions in cubic crystal fields with such small non-cubic distortions. The $B_2^0 = 12.47 \times 10^{-4}$ cm^{-1} value reported for both cases is close to the range of values determined by us. The rhombic B_2^2 term of the highest absolute value [30] was added in order to wipe out the non-central transitions. However, when making a simulation of the X-band spectrum by using their reported SH parameters we found out that the expected effect of the rhombic term is only partial, a complete smoothing of the non-central transitions still requiring the inclusion of line broadening effects.

Based on the reported hyperfine parameter values, which depend essentially on the nature and distribution of the first shell neighboring ligands [34], we would venture to state that the reported Mn^{2+} substitutional centers in cZnS NCs, i.e. NC1 [7], S_I [8], Signal I [10], samples 1, 2 [11] and I_b [12], are similar to our

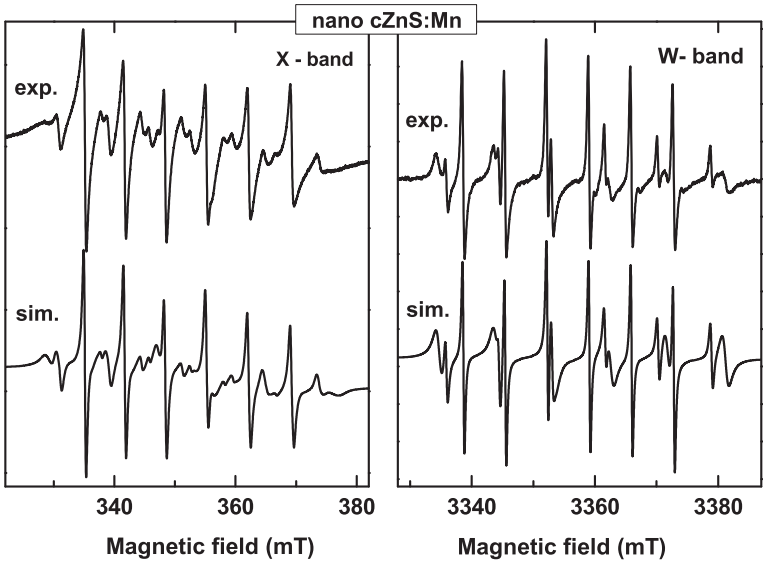

Fig. 5. Experimental X- (left) and W-band (right) EPR spectra of the cZnS:Mn nanopowders, together with the calculated spectra resulted from the summation of the simulated spectra of the three Mn^{2+} centers. The broad line from the agglomerates of Mn^{2+} ions was also included in the X-band spectrum simulation.

Mn(I) centers. In all cases the nanocrystals were small enough so that the main doping mechanism should be related with the presence of the stacking defects [18], which seems to be the determinant factor for the localization of the substitutional Mn^{2+} ions. The differences between the reported SH values do not seem to be due to the differences in the starting materials and preparation procedure, but rather to errors in the magnetic field calibration (for the *g*-parameters) and inaccuracy in the *ZFS* parameter determinations.

The SH parameters of some of the previously reported surface Mn^{2+} centers in cZnS nanocrystals are close enough to the *g*- and *A*-parameters of the Mn(II) and Mn(III) centers, but with larger axial *ZFS* parameter values (Table 1). This could be due to actual differences in the structure of the centers, resulting from different preparation procedures, including the NCs coating materials, but also to larger calculation error margins. According to Simanek and Mueller [34], the larger value of the hyperfine parameter of the surface Mn^{2+} centers compared to the substitutional Mn^{2+} center (Table 1) points to a more ionic environment for the Mn^{2+} ions on the NCs surface. This seems to result from bonding with oxygen and/or hydroxyl anions, similar to the case of manganese doped nanocrystalline ZnO and $Zn(OH)_2$ [35]. This hypothesis is also supported by our experiments which show the Mn(II) and Mn(III) centers transforming into each other by thermally induced desorption/adsorption of water molecules [18].

Previous X- and Q-band EPR investigations [7,10] have reported a glass-like behavior for the surface centers, with frequency dependent EPR line width according to the formula $\Delta B \approx D^2/g^2\beta^2 B_0$ [36]. Using this formula Kennedy et al. [7] have determined rather high values in the $(167–333)\times 10^{-4}\,cm^{-1}$ range for the $B_2^0 = D/3$ parameter of the NC2 surface centers in their methacrylic acid coated cZnS NCs.

Igarashi et al. [10] determined a $53.3 \times 10^{-4}\,cm^{-1}$ value for the B_2^0 parameter of the so called Signal II measured on poly(acrylic acid) coated cZnS NCs, by using Allen's method.

Two types of surface centers were reported by Gonzalez Beermann et al. [12] in the cZnS NCs samples Ih (0.191% Mn) and SD (0.027%), with similar *g*- and *A*-parameters, but with very different axial *ZFS* parameter values. The larger $B_2^0 = 124.6 \times 10^{-4}\,cm^{-1}$ value for the centers observed in the Ih sample, attributed to Mn^{2+} clusters in the near-surface sites, is close to the values reported in Ref. [7]. The smaller $B_2^0 = 46.7 \times 10^{-4}\,cm^{-1}$ value for the centers observed in the SD sample, attributed to Mn^{2+} isolated ions in the near-surface sites, is close to the value reported for Signal II in Ref. [10].

Based on the close *g*- and *A*-parameter values previously reported for the Mn^{2+} surface centers in cZnS NCs (Table 1), it seems very likely that the Signal II centers reported in Ref. [10] represent Mn^{2+} ions in the oxidized areas at the surface of the cZnS NCs, similar to the Mn(II) centers. Also, the NC2 centers reported in Ref. [7] and the S_{II} centers reported in Ref. [8] could be Mn^{2+} ions in hydrolyzed surface areas of the cZnS NCs, similar to the Mn(III) centers.

To our knowledge, EPR line broadening effects have not been previously analyzed in the case of the Mn^{2+} ions in cZnS NCs. Counio et al. [37] have used an approach similar to Allen's [33] to analyze the EPR spectra of the substitutional Mn^{2+} ions in CdS NCs, but they assumed a distribution of values of the *D*-parameter rather than a unique value. From the intensity ratio of the allowed central transitions they evaluated the half-width at half-height of the *D*-distribution as $\Delta D \approx 84 \times 10^{-4}\,cm^{-1}$. They attributed the local crystal field distribution correlated with the *D*-parameter distribution centered on a $D = 0$ value to the finite size of the nanocrystals.

3. Conclusions

The quantitative analysis of well resolved EPR spectra from Mn^{2+} impurity ions in small cubic ZnS:Mn nanocrystals self-assembled into a mesoporous structure, recorded in both low (X) and high (W) microwave frequencies, was performed using publicly available powerful computer programs for spectra line shape simulation and fitting, including the forbidden transitions and line broadening effects as well. Accurate SH parameters for the three isolated Mn^{2+} centers observed in this system were determined, resulting in a good fitting of the experimental spectra.

To our knowledge, this is the first reported case when the broadening mechanisms were evaluated for the EPR spectra of the Mn^{2+} ions in nanostructured cZnS. The resulting broadening parameter values, orders of magnitude higher than in the manganese doped cZnS SC [13], or even in the crystalline powder obtained from crushing such single crystals, reflect the much higher degree of disorder in the nanocrystals.

A comparison between the X-band EPR spectra of a cubic ZnS:Mn NC sample and of a micron sized powder sample obtained

by crushing a cubic ZnS:Mn SC allowed us to pinpoint the different localization and structure of the substitutional Mn^{2+} centers in the two systems, as well as the differences in the local lattice strains.

The analysis of the EPR spectra of the cubic ZnS:Mn NC with the presented approach lead to the following results and conclusions regarding the substitutional and surface Mn^{2+} centers.

In the case of the substitutional Mn(I) centers in cZnS:Mn NCs, whose spectra were the most intense and had the narrowest lines:

- Accurate *g*- and *A*-parameter values were determined from the high frequency spectrum, where the influence of the *ZFS* terms is negligible, while the second order axial *ZFS* parameter was determined from the X-band spectrum, where the forbidden transitions could be observed. The best fit with the experimental data was obtained for a negative value of the B_2^0 parameter.
- Limits for the *g*- and *A*-parameters anisotropies were determined as the maximum values for which the EPR line shapes were not distorted.
- Based on the accurate SH parameters thus determined it has been possible to explain the local axial distortion at the substitutional Mn^{2+} ions as resulting from their preferential localization next to extended stacking lattice defects [18].
- The line broadening effects due to strain induced fluctuations in the local crystal field at the Mn^{2+} ions sites were included as Gaussian distributions in the *ZFS* parameters. The width of these distributions was determined as the maximum value which would smooth out the non-central transitions.
- It was not possible to ascertain the presence of a local rhombic distortion described by a B_2^2 parameter, or to determine the fourth order *ZFS* parameters. The effects associated with the presence of such terms were hidden by the line broadening effects.
- We found out that the relative intensity of the experimental forbidden transitions *vs.* the allowed transitions was about two times larger than in the calculated spectrum, an effect previously observed in the case of the substitutional Mn^{2+} ions in cZnS SCs.

In the case of the two surface centers, Mn(II) and Mn(III), with lower intensity spectra and overlapping lines, we could still determine accurate *g*- and *A*-parameter values. Unfortunately, due to the absence of resolved forbidden transitions in the X-band spectrum we could determine only a range of tentative values for the B_2^0 parameter, for which the corresponding EPR line shapes and widths fitted reasonably well the experimental spectra. However, based on the resulting values of the hyperfine splitting parameters it was possible to get a better insight into their localization at the surface of the cZnS NCs.

The above described approach for the quantitative analysis of the Mn^{2+} centers in cubic nanocrystals represents a useful tool for extracting maximum information from the CW EPR spectra, enabling a more accurate determination of the localization of the paramagnetic impurities in these nanostructures, as well as of their ground state properties.

4. Experimental

The X- and W-band EPR spectra of Mn^{2+} ions in mesoporous, nanocrystalline cZnS doped with 0.2% mol manganese analyzed in this work have been previously reported in Ref. [18], where details regarding the investigated sample as well as the EPR experiments and instruments are reported.

We have also recorded and analyzed the X-band EPR spectrum of a micron sized polycrystalline sample obtained by crushing in an agate mortar a small single crystal of high quality cubic ZnS doped with 0.5% mol $MnCl_2$, taken from the same growth batch of single crystals which were thoroughly investigated by X-band EPR [13].

The analysis of all EPR spectra, including the determination of the SH parameters and the line shape analysis by simulations/deconvolutions, was performed with the SIM [38,39] and EasySpin v.3.1 [40] specialized programs. The line broadening effects due to parameter value fluctuations were included by employing the weighted summation procedure outlined in Ref. [41].

Acknowledgment

This work was supported by CNCSIS-UEFISCSU Project Number PN-II-ID-523/2008.

References

[1] S.C. Erwin, L. Zu, M.I. Haftel, A.L. Efros, T.A. Kennedy, D.J. Norris, Nature 436 (2005) 91–94.
[2] D.J. Norris, A.L. Efros, S.C. Erwin, Science 319 (2008) 1776–1779.
[3] H. Hu, W. Zhang, Opt. Mater. 28 (2006) 536–550.
[4] R.N. Bhargava, D. Gallagher, X. Hong, R. Nurmikko, Phys. Rev. Lett. 72 (1994) 416–419.
[5] A. Bol, A. Meijerink, Phys. Rev. B 58 (1998) R15997–R16000.
[6] J.R. Pilbrow, Transition Ion Electron Paramagnetic Resonance, Clarendon Press, Oxford, 1990.
[7] T.A. Kennedy, E.R. Glasser, P.B. Klein, R.N. Bhargava, Phys. Rev. B 52 (1995) R14356–R14359.
[8] P.H. Borse, D. Srinivas, R.F. Shinde, S.K. Date, W. Vogel, S.K. Kulkarni, Phys. Rev. B 60 (1999) 8659–8664.
[9] T. Igarashi, T. Isobe, M. Senna, Phys. Rev. B 56 (1997) 6444–6445.
[10] T. Igarashi, M. Ihara, T. Kusunoki, K. Ohno, T. Isobe, M. Senna, J. Nanoparticle Res. 3 (2001) 51–56.
[11] P.A. Gonzalez Beermann, B.R. Mc Garvey, S. Muralidharan, R.C.W. Sung, Chem. Mater. 16 (2004) 915–918.
[12] P.A. Gonzalez Beermann, B.R. Mc Garvey, B.O. Skadtchenko, S. Muralidharan, R.C.W. Sung, J. Nanoparticle Res. 8 (2006) 235–241.
[13] S.V. Nistor, M. Stefan, J. Phys.: Condens. Matter 21 (2009) 145408.
[14] Y.L. Soo, Z.H. Ming, S.W. Huang, Y.H. Kao, R.N. Bhargava, D. Gallagher, Phys. Rev. B 50 (1994) 7602–7607.
[15] W. Vogel, P.H. Borse, N. Deshmukhand, S.K. Kulkarni, Langmuir 16 (2000) 2032–2037.
[16] S.V. Nistor, L.C. Nistor, M. Stefan, C.D. Mateescu, R. Birjega, N. Solovieva, M. Nikl, Superlattices Microstruct. 46 (2009) 306–311.
[17] S.V. Nistor, L.C. Nistor, M. Stefan, D. Ghica, C.D. Mateescu, R. Birjega, Rom. Rep. Phys. 62 (2010) 319–328.
[18] S.V. Nistor, M. Stefan, L.C. Nistor, E. Goovaerts, G. Van Tendeloo, Phys. Rev. B 81 (2010) 035336.
[19] B. Lambert, T. Buch, B. Clerjaud, Solid State Commun. 10 (1972) 25–27.
[20] T. Buch, B. Clerjaud, B. Lambert, P. Kovacs, Phys. Rev. B 7 (1973) 184–191.
[21] A.Ya. Yakunin, I.V. Shtambar, A.S. Kushnir, S.A. Omelchenko, Russ. Phys. J. 16 (1973) 1375–1379.
[22] A. Abragam, B. Bleaney, Electron Paramagnetic Resonance of Transition Ions, Clarendon Press, Oxford, 1970.
[23] S.A. Marshall, A.R. Reinberg, Phys. Rev. 132 (1963) 134–142.
[24] G.E. Barberis, R. Calvo, Solid State Commun. 12 (1973) 963–965.
[25] G.E. Barberis, R. Calvo, H.G. Maldonado, C.E. Zarate, Phys. Rev. B 12 (1975) 853–860.
[26] S.V. Nistor, M. Stefan, E. Goovaerts, M. Nikl, P. Bohachek, Radiat. Meas. 38 (2004) 665–668.
[27] A.M. Stoneham, Rev. Mod. Phys. 41 (1969) 82–108.
[28] A. Nicula, I. Ursu, S.V. Nistor, Rev. Roum. Phys. 10 (1965) 229–237.
[29] H.W. De Wijn, R.F. Van Balderen, J. Phys. Chem. 46 (1967) 1381–1387.
[30] C.P. Poole Jr., H.A. Farach, W.K. Jackson, J. Chem. Phys. 61 (1974) 2220–2221.
[31] K.J. Standley, R.A. Vaughan, Electron Spin Relaxation Phenomena in Solids, Adam Hilger Ltd., London, 1969.
[32] J. Kreissl, Phys. Status Solidi A 97 (1986) 191–198.
[33] B.T. Allen, J. Chem. Phys. 43 (1965) 3820–3826.
[34] E. Simanek, K.A. Muller, J. Phys. Chem. Solids 31 (1970) 1027–1040.
[35] H. Zhou, D.M. Hofmann, A. Hofstaetter, B.K. Meyer, J. Appl. Phys. 94 (2003) 1965–1968.
[36] D.L. Griscom, R.E. Griscom, J. Chem. Phys. 47 (1967) 2711–2722.
[37] G. Counio, S. Esnouf, T. Gacoin, J.-P. Boilot, J. Phys. Chem. 100 (1996) 20021–20026.
[38] J. Glerup, H. Weihe, Acta Chem. Scand. 45 (1991) 444–448.
[39] C.J.H. Jacobsen, E. Pedersen, J. Villadsen, H. Weihe, Inorg. Chem. 32 (1993) 1216–1221.
[40] S. Stoll, A. Schweiger, J. Magn. Reson. 178 (2006) 42–55.
[41] J. Kliava, Phys. Status Solidi B 134 (1986) 411–455.